

**Global Ionospheric TEC Perturbations Monitored by the GPS Global
Network during Two Northern Hemisphere Winter Storms**

C. M. Ho, A. J. Mannucci, L. Sparks, X. Pi,
U. J. Lindqwister, B. D. Wilson, and M. J. Reyes

Jet Propulsion Laboratory,
California Institute of Technology, Pasadena, California

To be submitted to Special Issue
in *Journal of Geophysical Research*

First version on June 20, 1997
Second version on December 19, 1997

Abstract. The global evolution of two major ionospheric storms, occurring on November 4, 1993 and November 26, 1994, respectively, is studied using measurements of total electron content (TEC) obtained from a worldwide network of ground-based GPS receivers. The time-dependent features of ionospheric storms are identified on a global scale using TEC difference maps based on the percent change of TEC during storm time relative to quiet time. The onset of each ionospheric storm is indicated by the appearance of auroral/subauroral TEC enhancements which occur within one hour of the beginning of the geomagnetic storm main phase. Significant TEC enhancements ($> 100\%$) are observed in the winter northern hemisphere. The rate at which TEC enhancements appear is found to correlate with gradients in the Dst index. The large scale ionospheric structures identified during the storms are: (1) nightside auroral/subauroral enhancements which surround the auroral oval; (2) dayside (around noon) high latitude and middle latitude enhancements associated with traveling ionospheric disturbances, and (3) conjugate latitudinal enhancements. For the November 93 storm, a short positive phase (about 15 hours) is followed by a long negative phase (-60 hours). In the November 94 storm, we have identified the clear signature of a traveling ionospheric disturbance (TID) which propagated at a speed of ~ 460 m/s from $\sim 70^\circ$ N to $\sim 50^\circ$ N. The motion of this disturbance appears to conserve angular momentum.

1. Introduction

The response of the ionosphere to magnetic storms is important for understanding the energy coupling process between the Sun and the Earth and for forecasting space weather changes. An ionospheric storm is a global scale ionospheric disturbance of total electron content (TEC), electron peak density and peak height during a geomagnetic storm, resulting from different dynamical and chemical processes, such as energetic particle precipitation, changes of electric field and current systems, traveling atmospheric disturbances, thermospheric circulation and composition changes, etc. The competition of these factors makes ionospheric storms complicated. This study examines the global evolution of the ionosphere in response to two geomagnetic storms and identifies common features as reflected in large-scale TEC perturbations.

Based on observations over decades at individual sites or a chain of sites, knowledge about the morphology of ionospheric storms has accumulated, and the mechanisms that drive ionospheric storms have been assessed in great detail [e.g., Matsushita, 1959; Mendillo, 1971; Klobuchar et al., 1971; Lanzerotti et al., 1975; Essex et al., 1981; Prölss et al., 1991; Yeh et al., 1994; Buonsanto, 1995]. Thermospheric winds and electromagnetic fields are thought to be the two main drivers of ionospheric storms. At mid-latitudes, thermospheric winds are believed to play a dominant role in ionospheric density changes [Fuller-Rowell, 1994]. However, at lower latitudes, electric field effects cannot be neglected [Earle and Kelley, 1987]. Simultaneous ionospheric variations over large scales can result from (1) penetration to low altitude of magnetospheric electric fields or electric fields associated with ring current shielding in the storm-time outer plasmasphere, and (2) disturbance dynamo effects resulting from large thermospheric circulation changes [Fejer et al., 1983; Pi et al., 1993].

Ionospheric TEC enhancements tend to appear first in the high latitude region ($> 60^\circ$). The increased energy input at high latitudes due to Joule heating and particle precipitation generates pressure gradients which drive the equatorward neutral wind. The wind disturbance can propagate to middle and even low latitudes, when both pressure gradients and ion drag forces are in the same direction [Foster, 1993]. These enhancements correlate well with substorm auroral surges and the auroral electrojet (AE) index. Typically, the expansion of a polar ionization enhancement [Prölss et al., 1991] (evening or nighttime subauroral region increases) may be caused by a combined effect of wind and electric field.

Subsequent neutral compositional changes are responsible for a relative decrease in TEC [Prölss, 1987; Buonsanto and Fuller-Rowell, 1997].

An important phenomenon causing TEC enhancements at subauroral and mid-latitudes is the traveling atmospheric /ionospheric disturbance (TAD/TID) [e.g., Titheridge and Buonsanto, 1988]. Strong impulsive acoustic gravity waves may launch TIDs from high latitudes. A TID can consist of a wave-train of several packets of increased electron density or can be a single, non-periodic irregularity. Usually these events last a few hours. Typical TID propagation speeds are 300-600 m/s although a 1,300 m/s speed has been detected for large-scale TIDs [Prölss, 1987]. Their wavelengths vary from several hundred to one thousand kilometers. Occasionally strong TIDs can propagate across the equator from one hemisphere to the other. Large scale TIDs simultaneously starting from high latitudes in each hemisphere have also been observed [Hajkowicz, 1990].

Prolonged increases of TEC may be due to thermospheric circulation changes and enhanced equatorward winds. Wave-like disturbances with TID periods and wavelengths are sometimes observed in the middle latitude region. In the middle latitudes, the equatorward displacement of the nightside ionospheric trough may be attributed to westward electric fields. Electric field perturbations can also be produced through a disturbance dynamo process [Blanc and Richmond, 1980] after the convective electric field withdraws. The dusk effect associated with storm-enhanced plasma density is a distinct feature on the poleward edge of the mid-latitude region [Buonsanto, 1995].

In the low latitude and equatorial regions, most neutral wind effects are damped due to the small magnitude of the magnetic inclination angle [Buonsanto and Foster, 1993]. However, electric field penetration and disturbance dynamo effects, which are caused by ion drifts, may affect TEC in these regions [Fejer et al., 1983]. An eastward electric field can drive plasma upward, while a westward electric field can drive plasma downward [Yeh et al., 1994].

With the advent of simultaneous worldwide GPS measurements, it has become possible to form a global picture of the ionospheric TEC response to magnetic storms [Ho et al., 1996]. The GPS stations distributed worldwide receive dual-frequency signals from GPS satellites continuously. Based on the dispersion of the received signals, high resolution interpolated TEC maps or Global Ionospheric Maps (GIM) can be produced as often as every 15 minutes [Mannucci et al., 1994; 1997]. Using these maps, we can analyze the

global evolution of ionospheric storms on temporal and spatial scales that have been difficult, if not impossible, to study previously.

In this study, we will use measurements from the GPS network to examine the global signatures of ionospheric TEC during two northern hemispheric winter storms: November 4, 1993 and November 26, 1994. Because both storms were long-lived events, associated with the occurrence of rotating coronal holes, the storms have received extensive attention in the space physics community. Using difference maps that compare storm-time and quiet-time TEC, we will investigate the ionospheric response to both storms, including the onset, development, and decay of TEC variations. On the basis of the classification of features, we will suggest possible generation mechanisms for each storm pattern. Results from GPS data will be compared to measurements from ionosondes and satellite instruments.

2. Data and Method of Analysis

The GPS constellation consists of 24 satellites at 20,200 km altitude ($4.2 R_e$ from the center of Earth). These satellites continuously broadcast dual-frequency signals for navigation purposes. The signals from the satellites pass through the ionosphere to reach ground-based GPS receivers. Each station continuously receives dual-frequency signals from as many as 9-10 GPS satellites simultaneously. The dispersion or time delay between the two frequency signals provides a measure of the integrated TEC along the entire propagation path.

The GIM method is a relatively new ionospheric retrieval technique based on data from a global network of GPS stations [Wilson et al., 1995; Mannucci et al., 1994 and 1997]. The method used here models the ionosphere using an infinitesimal thin shell at a fixed altitude. The slant TEC along the ray path is projected vertically at the point where it intersects the shell. Line-of-sight TEC values T_{rs} between any receiver and satellite are modeled with the following expression:

$$T_{rs} = M(E) \sum_i W_i(\theta, \phi) V_i + b_r + b_s \quad (1)$$

where $M(E)$ is the geometric mapping function, E is an elevation angle, $W_i(\theta, \phi)$ is a basis function defined at ionospheric penetration point i at latitude θ and longitude ϕ , V_i is the vertical TEC at a set of grid vertex points, and b_r and b_s are the instrumental biases in

receivers and satellites, respectively. The optimal ionospheric shell height has been determined by adjusting the mapping function and comparing results with independent TEC measurements from the TOPEX altimeter [Imel, 1994]. During any interval, the data coverage in the maps depends only on the distribution of available satellites and receivers. For example, Figure 1 shows the trajectories of the ray paths intersecting the ionospheric shell over a six hour interval during the November 93 storm. The addition of new stations in sparsely populated regions resulted in improved data coverage during the November 94 storm.

A sophisticated Kalman-type filter is used to estimate instrument biases and TEC values at grid points on the spherical shell. Grid points are fixed in a solar-geomagnetic coordinate system since the ionosphere changes less over time in a local time reference frame [Mannucci et al., 1994 and 1997]. We initialize the shell vertex values with an empirical ionospheric model. Because the map is relatively insensitive to the particular model used, the Bent model [Bent et al., 1976], which can be computed in less time than other models, was selected for this study. Measured TEC values are used to update estimates and covariances every hour (in this study) for each of 642 vertex values distributed evenly over the globe. Grid TEC values are treated in the Kalman filter as stochastic parameters, meaning that their uncertainty grows with time until a new measurement becomes available. For most grid points residing in a given geomagnetic latitude band, measurements become available as stations rotate in the local time coordinate system. A measurement recorded at a given station may persist for several hours in a (local time) region of sparse data until a new station passes into this region. TEC values at arbitrary positions are evaluated using linear interpolation between the 642 vertices. Accompanying the global TEC map, a TEC error map is also generated simultaneously [Mannucci et al., 1994; 1997]. Comparison with independent TOPEX data indicates that the typical rms error is less than 5 TECU (1 TECU = 10^{16} electron/m²) in global regions less than 1500 km from a station [Ho et al., 1997].

To identify TEC variations during storms, including the motion, expansion, and intensity of disturbed regions, difference maps are computed to show the percent change of storm-time TEC relative to TEC maps averaged under quiet conditions. Large percent changes in TEC are interpreted as significant enhancements or depletions characteristic of storm behavior. In this study, the quiet-time TEC maps are computed for each UT hour by averaging 5 days of GIMs taken from the low magnetic activity period just prior to each storm. The standard deviation (σ) of TEC over a 2 x 2 degree grid is also computed, indicating the magnitude of daily fluctuations during quiet time.

We calculate percent change rates (γ) of the storm-time TEC (α) relative to the quiet-time average TEC (β) as follows. If the difference between the two values is less than the standard deviation of the quiet-time fluctuations (that is, $|\alpha - \beta| < \sigma$), then the change is ignored ($\gamma = 0$). If $|\alpha - \beta| > \sigma$ (the difference between the two values is greater than the standard deviation of the quiet-time fluctuations), then $\gamma = (\alpha - \beta - \sigma)/\beta$ when $\alpha - \beta > 0$ and $\gamma = (\alpha - \beta + \sigma)/\beta$ when $\alpha - \beta < 0$. In this manner, we reduce the contamination of non-storm variations from consideration. The quiet-time fluctuations in the low latitude and equatorial regions (σ can be as high as 15 TECU) are usually larger than those in other regions. If we do not establish this threshold, there are many scattered enhancements or depletions, especially in the low latitude and equatorial regions, even during quiet time. A consequence of our approach, however, is that low latitude storm effects are more difficult to distinguish from the large quiet-time "noise".

3. Results

Since high speed coronal mass ejections occur less frequently during the solar declining phase, corotating high speed streams accompanying IMF sector reversals are the dominant sources of geomagnetic activity at the storm periods under consideration here. Solar flux decreased from a maximum ($F_{10.7} = 243$, sunspot number = 176) in 1991 to a minimum ($F_{10.7} = 77$, sunspot number = 6) in 1996. Peak TEC values in the equatorial region also decreased from 130 to 38 TECU. Even near solar minimum, however, ionospheric changes during storm time can be significant relative to the quiet time. In this study, both the November 93 and November 94 storms occurred when a change in the IMF polarity from inward to outward coincided with the leading edges of corotating interacting streams. Both storms were long-lasting northern hemispheric winter storms; the Dst index in each case took more than six days to recover to its quiet-time values.

3.1. November 93 Storm. The evolution of ionospheric TEC during the magnetic storm of November 3, 1993 was measured by more than 40 GPS stations. The stations and their locations during 1993 and 1994 are listed in Table 1. The storm commenced suddenly at 1720 UT on November 3. At 2100 UT the IMF detected by IMP-8 showed a southward turning; its B_z component reached a minimum (-35 nT) after two hours. K_p reached 7- in the first three hours of November 4. At 0500 UT on November 4, the Geotail spacecraft, located in the distant magnetotail at (-206, -18, 3 Re) in the GSE coordinate system, detected solar wind speeds up to 700 km/s (compared with 275 km/s on the previous day).

The Dst index dropped to a minimum (105 nT) at 0700 UT and after a slight recovery, dropped to another minimum (-116 nT) five hours later. At 0300 UT on November 5, the Dst index started to recover. Figure 2a shows the Dst index for this storm (for complete AE and Dst indices, we refer readers to the article of D. Knipp et al., in this issue). During the storm interval, the global ionospheric peak TEC in the maps varied from 64 to 126 TECU, while the solar flux (F10.7) was around 96×10^{-21} Joules s⁻¹ m⁻² Hz⁻¹.

Figure 3 shows an averaged global ionospheric TEC map obtained under quiet-time conditions. This map gives the TEC distribution between 00 and 01 UT derived from a 5 day average (Oct. 29 through November 2) over the period immediately proceeding the storm day. These 5 days also exhibit quiet magnetic activity. Thus, this map (and similar ones obtained for other UT hours) can serve as a quiet-time reference ionosphere. GPS stations are identified as white dots. The map is shown in a geomagnetic coordinate system (geomagnetic latitude vs. magnetic local time) because we expect the main ionospheric features to be ordered by the geomagnetic field. Local noon is in the middle while the Earth rotates from left to right. The dashed black lines give geographic coordinates, while the white lines show geomagnetic coordinates. The absolute TEC scale is shown on the right side color bar. The expected position of the storm-time auroral oval is also shown in both polar regions. No data were available above 80° geographic latitude. We can observe several large-scale features of the global ionosphere. The peaks of the equatorial anomaly can be observed on either side of the equator, and the middle latitude troughs appear at $\pm 60^\circ$. The equatorial anomaly peak is larger on the southern hemispheric side of the equator than on the northern side, since summer is occurring in the southern hemisphere during this period.

Figure 4 shows a storm-time global ionospheric TEC map measured between 0500-0600 UT, November 4, 1994. Compared with the previous quiet-time map, the peaks of the equatorial anomaly are now closer to the geomagnetic equator. The maximum TEC value is about 80 TECU. During this hour, we also see an enhancement near Australia around 30°S and some disturbances in the nightside.

In Figures 5a, b, and c, we present global TEC difference maps for three separate hours during the storm. Each difference map shows the percent change of storm-time TEC relative to the quiet-time average as defined in Section 2. Ionospheric TEC increases in the northern hemisphere subauroral latitude (60°N) between 0000 UT and 0100 UT on November 4 during the beginning of the magnetic storm main phase (Figure 5a). Several

enhancement regions appear, for example, over Alaska (local time noon) and the northern US (evening sector 18-21 LT). During the same period, an enhancement appears in the southern hemisphere around New Zealand ($\sim 50^\circ\text{S}$) between 10-12 LT. All of these TEC enhancements represent an increase of more than 100% relative to the quiet time.

All of the TEC enhancement regions expand during the next few hours. From 10 - 22 LT and between 50°N and 70°N in geomagnetic latitude, several enhancements cover Northern America to form a wide auroral/subauroral enhancement band. The southern hemispheric enhancement spreads into Australia around local noon. Three hours later, the northern auroral enhancement reaches its maximum. As shown in Figure 5b, at 0700-0800 UT, the northern auroral band shifts from dayside to nightside, accompanying the Earth's rotation. It should be noted, however, that the large enhancement in northern Russia is due to the persistence of previous measurements in Alaska rotating into a region where there are no GPS receivers (as discussed in Section 2).

The negative phase of the ionospheric storm is initially detected 15 hours after the geomagnetic storm main phase. Severe depletions (~ -50 to -80%) are observed in the evening sector (European sector) in the northern hemisphere between 50°N and 70°N as seen in Figure 5c. Some of the enhancements in the nightside persist into the second day. The negative phase lasts more than 60 hours. It is not until November 10 that the ionosphere completely recovers. In short, this is an ionospheric storm with a positive phase followed by a negative phase and then a slow recovering phase.

In Figure 2a, we have identified the largest TEC enhancement in each difference map (i.e., each hour) by a cross symbol, where the size of the symbol corresponds to the magnitude of the enhancement. In Figure 2b we have shown a histogram of the occurrence rate for TEC enhancements, using a threshold of $>60\%$ as a selection criterion. One can see that occurrence rate is larger where the change in the Dst index is large.

We have also used independent ionospheric measurements from satellite and ground stations to examine these storm changes. The ionospheric absolute TEC values from GIM and the TOPEX altimeter during storm time are plotted in Figure 6. On November 4, 1993, TOPEX followed trajectories starting from the southern Pacific Ocean, passing through the eastern Pacific Ocean, crossing the continental US, and then ending in Greenland. We see that the interpolated TEC values from GIMs follow the measurements from TOPEX reasonably well. During this interval (0738 - 0832 UT), along the path of TOPEX, there

are an enhancement ($>100\%$) in the southern Pacific Ocean ($20\text{--}40^\circ\text{S}$), a depletion ($\sim 30\%$) between 10°S and 10°N , and a subauroral enhancement near Greenland (60°N), relative to previous quiet days. These TEC features are evident in GIMs and in measurements from TOPEX (see Figure 6), and they can also be identified in the TEC difference map (Figure 5b). In Figure 6, we have also plotted TEC values predicted from the Bent model along the TOPEX track. Note that this climatological model significantly under-estimates the TEC profile and does not follow the TEC enhancement present during storm time.

A direct comparison of global ionospheric TEC maps with ground-based ionosonde N_mF_2 measurements is shown in Figure 7a and 7b. We have selected the ionosonde station chain at 15°E geographic longitude ($LT = UT + 01$) in northern Europe, because it has large latitudinal coverage. Data are compared for four days (November 3 through 6) as functions of universal time. In this case, no GPS stations are co-located with the ionosonde stations (see the map in Figure 3 for the locations of GPS receivers). TEC values at the geomagnetic latitudes of the ionosonde stations are obtained by interpolating measurements from nearby GPS stations (automatically accomplished via the GIM approach). Starting at 1700 UT of November 3 (Figure 7a), N_mF_2 measurements are not available since intense absorption of ionosonde signals occurred. However, from sporadic data, we can still see an enhancement of N_mF_2 in the nightside after the storm onset. Correlation coefficients between N_mF_2 and TEC at each latitude are calculated and are shown in the figure. The correlation between measurements is quite high (from 0.60 to 0.92), but note that TEC profiles measured from GIMs have large fluctuations at high latitudes. At middle latitudes (around station Rome), the GIM measurement shows a large TEC peak at 0800 UT on the 4th, while ionosonde data do not indicate a corresponding feature. (However, TEC is an integrated density that averages over many layers.) The negative phase for both TEC and N_mF_2 begins at these stations after 1300 UT of November 4. In subsequent days, both GIM and ionosondes detect low electron densities relative to the quiet day (November 3). GIM measurements are generally consistent with those from ionosonde stations.

With global ionospheric TEC maps, continuous TEC perturbations in a particular longitude sector can be studied. In Figure 8, we have plotted the percent TEC changes at the Greenwich meridian in the northern hemisphere averaged over a 10° latitude band. The enhancements at high latitudes of the northern hemisphere start after the storm onset (solid vertical line). The positive phase is very strong ($\sim +100\%$ in the $60^\circ\text{--}70^\circ\text{N}$ band). A negative phase occurs on the second day and lasts more than one day in this longitude sector. Both

phases are seen mainly above 50°N. Positive and negative changes do not exceed $\pm 50\%$ below 50°N latitude .

3.2. November 94 Storm. The magnetic storm occurring on November 26, 1994 was also a recurrent major storm. Observations from the WIND spacecraft (Lepping, 1997) upstream from the Earth indicate a large variation of the interplanetary magnetic field B_z component at 0600 UT, associated with a high speed solar wind stream and a magnetically compressed region. The minimum IMF B_z reached -23 nT during this interval. Figure 9a shows the variation of the Dst index over the storm period. The ground magnetic field measurements show that a sudden commencement occurred at ~ 0700 UT, while the main phase of the storm started at 0900 UT. At 1300 UT the Dst index reached its minimum value of -122 nT and then the IMF B_z turned northward. The maximum Kp was 6⁺ in the 0900-1200 UT interval. The storm recovered slowly, taking six days to return to normal. During this period, solar F10.7 was 83×10^{-21} Joules s⁻¹ m⁻² Hz⁻¹, near its minimum value over the solar cycle. The global maximum TEC values varied from 47 to 76 TECU.

Global ionospheric TEC perturbations were recorded by more than 50 GPS stations during this storm. Because the response of the ionosphere took place mainly in the northern hemisphere, we will use north polar view maps to show the ionospheric TEC changes. Figures 10a, b, c, and d show TEC difference maps for four sequential hours. The maps give the storm-time percent changes relative to the average quiet-time base from the previous 5 quiet days (November 21 - 25). During these days, the daily sum of hourly Dst index values is less than 15 nT. We have also delineated the expected location of the storm-time auroral oval using white ellipses.

The ionospheric enhancement onset at high northern latitudes occurs after the magnetic storm main phase starts. From the northern hemispheric map, we can see that at least three enhanced regions are present in the interval 0900-1000 UT (Figure 10a) at or near subauroral latitude $\sim 60^\circ$ N. One is in the pre-dawn (03 LT) sector, another is in the morning sector 09-12 UT (later identified as the signature of a traveling ionospheric disturbance that survives until 1600 UT), while a third is in the post-dusk sector (20-23 LT). The polar view reveals that these auroral/subauroral enhancements nearly coincide with the auroral oval, exhibiting slight equatorward displacement.

At 1100 UT (Figure 10b) the enhancements located in the dayside (around noon) and predawn become large. The dayside enhancement shows a clear equatorward extension.

The predawn enhancement spreads into the morning side, while low latitude enhancements also spread into the nightside between 20° and 40°N latitude. At 1300 UT (Figure 10c) all enhancements reach their maximum, coincident with the maximum deviation in the Dst index. The southern edge of the dayside peak has extended down to 30°N. In addition, three enhancements in the ~21 LT sector (of which only two are visible in Figure 10c), separated by ~40° in latitude, form a well defined latitudinal structure extending from the northern hemisphere to the southern hemisphere (also seen in Figure 11).

At 1500 UT (Figure 10d) dayside enhancements begin to decay, while other high and midlatitude ones remain strong. The nightside subauroral enhancement remains, while other middle and low latitude enhancements persist until 2200 UT. Starting from 1500 UT, enhancements also appear at the conjugate geomagnetic latitude of the southern hemisphere, but the enhanced regions are weaker than those in the northern hemisphere (see Figure 11). These conjugate enhancements are seen in the post-midnight sector around 60° geomagnetic latitude. In the northern hemisphere the negative phase for this storm is negligible, but in the southern hemisphere, there is a weak decrease during second day.

In Figure 9a, we have used the cross symbols to show the magnitude of the largest enhancement at each UT hour; a histogram of the enhancement occurrence rate is shown in Figure 9b. Compared with the November 93 storm, there are many more enhancements with large magnitude. A correlation between the Dst index gradients and TEC enhancements is evident. These enhancements generally occur whenever the Dst index exhibits a sharp gradient, even at times other than the storm main phase. This suggests that these enhancements bear some relation to high latitude substorm activity.

We have also compared GPS TEC measurements with ionosonde N_mF_2 measurements at the same northern European stations as used to study the 1993 storm. Comparisons are made over three days (November 25 - 27) of the storm period as shown in Figure 12. Comparing data of November 25 to data of November 26, it appears that enhancements in TEC are coincident with enhancements in N_mF_2 during the storm. On November 26 (the storm day), TEC profiles measured from GIMs have maxima at the same times as the maxima of N_mF_2 at the three ionosonde stations. Note that these peaks show a clear shift from high latitudes to low latitudes within a three hour interval. Also note that the F_2 layer peak heights h_mF_2 measured at three stations at the same time increase about 35 km. These facts suggest that a traveling ionospheric disturbance is propagating from high latitude (62°) to middle latitude (42°) regions and pushes plasma to higher altitude. Based on the

observed shift in peak position, the propagation speed of the TID is about 460 m/s. However, the ionosonde data shows more variation than the GIMs. This may be due to the smoothing and interpolation inherent in the GIM technique. Note that at higher latitudes (e.g., at station Lycksele), there is strong ionospheric absorption during the storm. Correlation coefficients between N_mF_2 and TEC measurements are shown in the figure for each latitude.

4. Discussion

In both northern hemisphere winter ionospheric storms, significant TEC enhancements are seen first in the northern hemisphere. The fact that we observe fewer enhancements in the southern hemisphere could be due to the lack of data coverage. However, asymmetry in TEC enhancements between the northern and southern hemispheres has been observed in previous studies. Positive perturbation usually prevails in the winter hemisphere. For example, Essex et al. [1981] examined a summer storm (northern hemisphere) and also found that the TEC enhancements were large in the winter (southern) hemisphere. Depletions in TEC are generally more severe in the summer hemisphere. Prölss and Zahn [1977] showed that in summer, thermospheric disturbances related to the negative phase of an ionospheric storm may extend to lower latitudes. In the summer, a large N_2/O density ratio can extend into lower latitude because of seasonal winds. Schodel et al. [1974] found that the storm of December 17, 1971 had the largest positive (by factors of 2-3) phase ever recorded at many of the individual ionosonde stations in the northern hemisphere, whereas the southern hemisphere showed substantial depletions in TEC. For the November 93 storm, however, a significant negative phase is seen in the northern high latitude region. The November 94 storm does not have an obvious negative phase. As expected, neither storm shows a large negative phase in the southern summer hemisphere. To understand these phenomena fully, we need to consider a superposition of storm circulation and quiet-time winter winds in relation to both particle heating intensity and neutral atmospheric circulation patterns. Such a study is beyond the scope of this paper.

We find for both storms that ionospheric TEC onset occurs within one hour of the start of the magnetic storm main phase. However, the time intervals from the magnetic storm onset differ for the two storms. Since the ionospheric storm and the magnetic storm have different drivers, the ionospheric storm onset is not necessarily correlated with the magnetic storm main phase. The ionosphere requires a delay time to transfer electromagnetic energy or particle energy into photo-chemical energy. This time includes the ion drift time and the

chemical reaction time. Each enhancement/depletion in TEC should correspond to energy dissipation or transport in the ionosphere. Electromagnetic energy deposited into the polar region will be transferred into thermal energy, kinetic energy and potential energy. A quantitative investigation of this energy budget is a topic for future study.

Typical features of the two storms are:

1. Auroral/subauroral enhancements. These enhancements appear mainly in the nightside between 50° - 70° in geomagnetic latitude, an auroral/subauroral latitude band, and they are common signatures for both storms. They generally coincide with the auroral oval around the geomagnetic pole but with slight equatorward displacements. The enhancements usually appear as the first indication of the storm onset and the final signature of the positive phase. These storm phenomena may be attributed to the expansion of polar ionization due to auroral particle precipitation and to an equatorward displacement of the polar side wall of the middle latitude trough, at least 10° from its original location (near 60° geomagnetic latitude) during quiet time [Prölss et al., 1991]. During the storm, electromagnetic energy and energetic particle precipitation in the polar region cause additional ionization. Thus, in the region where the quiet-time trough is located, there is a large percent TEC increase (often $> 100\%$).

2. TID/TAD. Electromagnetic coupling, particle precipitation and auroral heating cause the polar atmospheric pressure to increase. Gravity waves can launch and drive large-scale traveling ionospheric disturbances from high to low latitudes. At middle latitudes equatorward propagating waves can drive F region plasma along field lines to higher altitude, where the chemical loss is much smaller, causing TEC and N_mF_2 to increase. As noted previously, the November 26, 1994 dayside enhancement with a clear equatorward expansion may be identified as the signature of a TID. Figures 10a - 10d show the TID starting, expanding, propagating equatorward, damping, and disappearing near 50° N.

The trajectory of the TID peak is displayed in Figure 13. The data points with error bars show the location of the TID peak as estimated from a visual inspection of a sequence of hourly TEC difference maps. To facilitate locating the position of the peak accurately, each difference map was replotted using a data range of $[-100\%, 250\%]$ rather than $[-100\%, 100\%]$. The error bars in Figure 13 provide an estimate of the uncertainty in the peak longitude. The uncertainty in the observed latitude (not shown) is roughly comparable to the uncertainty in the observed longitude at each point.

The angular momentum of the primary TID appears to be approximately conserved as it propagates. An object which conserves angular momentum while moving from high to low latitude on the surface of a globe, satisfies

$$L = m \omega(t) r \cos(\theta(t)) = \text{constant} \quad (2)$$

where m is the object mass, $\omega(t)$ is its angular velocity about the rotation axis as a function of time, r is the radius of the sphere and $\theta(t)$ is the object latitude as a function of time. The change in longitude as a function of time may be obtained by integrating $\omega(t) = d\phi(t)/dt$:

$$\phi(t) - \phi_0 = k \int_{t_0}^t \frac{dt}{\cos(\theta(t))} \quad (3)$$

where $k = L / mr$. We test the observed TID trajectory for angular momentum conservation by comparing it to a trajectory calculated using equation (3) and the observed $\theta(t)$. Noting that the observed change in $\phi(t)$ over the six-hour period of TID propagation is $\sim 54^\circ$, we first evaluate equation (3) using the modified trapezoidal rule to obtain $k = 4.69$. Once k has been defined, we can evaluate equation (3) repeatedly at different times t to define, within an integration constant ϕ_0 , a TID trajectory that conserves angular momentum. The dashed curve in Figure 13 represents the trajectory when ϕ_0 , the initial TID geographic longitude, is set equal to 18° . The dotted curve in Figure 13 represents the trajectory that the TID would have followed if it had remained at fixed local time while moving southward according to the observed $\theta(t)$. The level of agreement between the observed data points and the calculated trajectory (dashed curve) indicates that the TID trajectory approximately conserves angular momentum. (Note: when evaluating the level of agreement between the two trajectories, it is sufficient to consider only the longitude error bars; latitude error bars are irrelevant since the dashed curve is calculated using the observed peak latitudes and any change in one or more of these values will modify the position of the dashed curve.) Thus, we may infer that the Coriolis force plays a dominant role in its propagation.

3. Conjugate latitude structure. The phenomena of TEC enhancement at conjugate geomagnetic latitudes has been noted in many previous studies [e.g., Tanaka, 1979]. This appears to have a magnetospheric origin. In the November 94 storm, we see conjugate enhancements around midnight at high latitudes. Also, the enhancement at northern latitudes is much stronger than that at southern latitudes. This may be caused by a plasma

flux transfer from the plasmasphere or the upper ionosphere. A magnetospheric electric field may squeeze plasma at high altitude toward the footprints of magnetic field lines. This plasma flux is not necessarily symmetrical about both hemispheres [Tanaka, 1979].

4. Negative phase. During the recovery phase, the negative phase of the storm is mainly due to ionospheric composition change. Recent study shows that thermospheric composition changes play an important role in plasma density changes [Buonsanto and Fuller-Rowell, 1997]. The neutral gas composition changes bring more N_2 to higher altitude after intensive ionospheric heating for many hours. The N_2/O ratio increase leads to an increase of chemical loss by ionization and thus a negative phase at middle latitudes. Composition changes are produced by a divergent neutral wind mainly in the region of Joule heating. During the November 93 storm recovery phase, we see a clear depletion process which expands from high latitude to middle latitude and from daytime to nighttime (as shown in Figure 5c or after). This negative storm effect may be caused by perturbations of the neutral gas composition. A large scale circulation in the thermosphere driven by high latitude heating has been considered as the source of the molecular enriched atmosphere [Prölss, 1987; Fuller-Rowell et al., 1994]. However, we do not exclude the possibility that the nightside high latitude depletions are caused by a displacement of the middle ionospheric trough.

5. Summary

We have used TEC measurements from a worldwide network of ground-based GPS receivers to study the global evolution of two major ionospheric storms, occurring on November 4, 1993 and November 26, 1994, respectively. We have identified large-scale storm-time features of the ionosphere in TEC difference maps based on the percent change of TEC during storm time relative to quiet time. Among these features are: subauroral enhancements, dayside mid-latitude enhancements, TID/TAD, latitudinal structures, negative phase depletions, and conjugate latitude enhancements. For both storms, we have compared GIMs with TOPEX satellite and ionosonde data and have found good agreement.

During both magnetic storms, ionospheric disturbances appear mainly in the high and middle latitude regions. Significant TEC enhancements, observed primarily in the northern hemisphere, expand from high latitude into lower latitude and also from nightside into dayside. Auroral/subauroral ionospheric enhancements nearly coincide with the auroral oval location but with a slight equatorward displacement. We find a correlation between

gradients of the Dst index and global ionospheric TEC changes. This correlation suggests that high latitude substorms affect the ionosphere through a direct (possibly electromagnetic) coupling process.

For the November 93 storm, ionospheric TEC increases at the beginning of the magnetic storm main phase. The ionospheric storm consists of both positive (TEC increases $>+100\%$) and negative (TEC decreases $< -60\%$) phases. In the northern hemisphere, the TEC increase is significant at high latitude and subauroral regions from noon to midnight. In the southern hemisphere, the increase is mainly seen in the middle latitude. A relatively short positive phase (about 15 hours) is followed by a long lasting negative phase (~60 hours). Depletions spread from dayside to nightside and from high to low latitude. The most severe decrease occurs in the daytime sector in the northern hemisphere.

For the November 94 storm, three ionospheric TEC enhancements first appear at subauroral latitudes following the storm main phase. Among them, two enhancements in the nightside are located respectively in the predawn sector and post dusk sector, while another occurs near dayside noon. The nightside enhancements are subauroral region features which persist for the entire storm period. The dayside enhancement, identified as a TID, travels toward the equator over a six-hour period. The motion of this disturbance appears to conserve angular momentum. The November 94 storm shows almost no negative phase.

Using GPS measurements to study the ionosphere offers several unprecedented advantages over more traditional means: (1) simultaneous global coverage, (2) high temporal resolution, (3) continuous coverage in time, and (4) readily accessible data. In this way global ionospheric TEC maps represent a powerful new tool for helping us to understand and to monitor ionospheric storm evolution processes.

Acknowledgments: We wish to thank Ruth Hobson of National Geophysical Data Center for providing ionosonde data, Dr. Delores Knipp for her coordinating work in this community storm study, and Anil Rao for his assistance in algorithm development. We also wish to thank the two referees of this paper whose careful reading of the original manuscript and considered criticism led to many improvements in our exposition. The research conducted at the Jet Propulsion Laboratory, California Institute of Technology was performed under contract to the National Aeronautics and Space Administration.

References

- Bent, R.B., S.K.Llewellyn, G.Nesterczuk, and P.E.Schmid, The development of a highly successful worldwide empirical ionospheric model, in *Effect of the Ionosphere on Space Systems and Communications*, edited by J.Goodman, 13-28, Nat.Tec. Inf. Serv., Springfield, Va., 1976.
- Blanc, M., and A.D.Richmond, the ionospheric disturbance dynamo, *J. Geophys. Res.*, 85, 1669, 1980.
- Buonsanto, M.J., A case study of the ionospheric storm dusk effect, *J. Geophys. Res.*, 100, 23857, 1995.
- Buonsanto, M.J., and T.J. Fuller-Rowell, Strides made in understanding space weather at Earth, *EOS Trans. AGU*, 78, 1, 1997.
- Buonsanto, M.J., and J.C.Foster, Effects of magnetospheric electric fields and neutral winds on the low-middle latitude ionosphere during the March 20-21, 1990, storm, *J. Geophys. Res.*, 98, 19133, 1993.
- Earle, G.D., and M.C.Kelley, Spectral studies of the sources of ionospheric electric fields, *J. Geophys. Res.*, 92, 213, 1987.
- Essex, E.A., et al., A global response of the total electron content of the ionosphere to the magnetic storm of 17 and 18 June 1972, *J. Atom. Terr. Phys.*, 43, 293, 1981.
- Fejer, B.G., M.F.Larsen, and D.T.Farley, Equatorial disturbance dynamo electric fields, *Geophys. Res. Lett.*, 10, 537, 1983.
- Foster, J.C., Storm time plasma transport at middle and high latitudes, *J. Geophys. Res.*, 98, 1675, 1993.
- Fuller-Rowell, T.J., et al., Response of the thermosphere and ionosphere to geomagnetic storms, *J. Geophys. Res.*, 99, 3893, 1994.
- Hajkowicz, L.A., A global study of large scale traveling ionospheric disturbances (TIDs) following a step-like onset of auroral substorms in both hemispheres, *Planet Space Sci.*, 38, 913, 1990.
- Ho, C.M. et al., Global ionosphere perturbations monitored by the worldwide GPS network, *Geophys. Res. Letts.*, 23, 3219, 1996.
- Ho, C.M., et al., A comparative study of the ionospheric TEC measurements by GIM with TOPEX and Bent model, *Radio Science*, 32, 1499, 1997.
- Imel, D.A., Evaluation of TOPEX/Poseidon dual-frequency ionosphere correction, *J. Geophys. Res.*, 99, 24895, 1994.
- Kelley, M.C., B.G.Fejer, and C.A.Gonzales, An expansion for anomalous ionospheric electric fields associated with a northward turning of the interplanetary magnetic field, *Geophys. Res. Lett.*, 6, 301, 1979.

- Klobuchar, J.A. et al., Ionospheric storm of March 8, 1970, *J. Geophys. Res.*, 76, 6202, 1971.
- Lanzerotti, L.J., L.L.Cogger, and M.Mendillo, Latitude dependence of ionosphere total electron content: Observations during sudden commencement storms, *J. Geophys. Res.*, 80, 1287, 1975.
- Lepping, R. , private communication, 1997.
- Mannucci, A.J., B.D.Wilson, and D.N.Yuan, Monitoring ionospheric total electron content using the GPS global network and TOPEX/Poseidon altimeter data, *Proceedings of the beacon satellite symposium*, Edt. by L. Kersley, pub. by Univ. Wales, Aberystwyth, UK, p338, 1994.
- Mannucci, A.J., B.D.Wilson, D.N.Yuan, C.M.Ho, U.J.Lindqwister and T.F.Runge, A global mapping technique for GPS-driven ionospheric TEC measurements, *Radio Sci.*, 1997, in press.
- Matsushita, S., A study of the morphology of ionospheric storms, *J. Geophys. Res.*, 64, 305, 1959.
- Mendillo, M., Ionospheric total electron content behavior during geomagnetic storms, *Nature*, 234, 23, 1971.
- Pi, X., M. Mendillo, M.W.Fox, and D.N.Anderson, Diurnal double maxima patterns in the F region ionosphere: Substorm-related aspects, *J. Geophys. Res.*, 98, 13677, 1993.
- Prölss, G.W., Storm-induced changes in the thermospheric composition at middle latitudes, *Planet. Space Sci.*, 35, 807, 1987.
- Prölss, G.W., and U. von Zahn, Seasonal variations in the latitudinal structure of atmospheric disturbances, *J. Geophys. Res.*, 82, 5629, 1977.
- Prölss, G.W., et al., Ionospheric storm effects at subauroral latitudes: A case study, *J. Geophys. Res.*, 96, 1275, 1991.
- Schodel, J.P., et al., A global description of the F-region during the ionospheric storm of 17 December 1971, *J. Atmos. Terr. Phys.*, 36, 1121, 1974.
- Tanaka T., The worldwide distribution of positive ionospheric storms, *J. Atmos. Terr. Phys.*, 41, 103, 1979.
- Titheridge, J.E., and M.J.Buonsanto, A comparison of northern and southern hemisphere TEC storm behavior, *J. Atom. Terr. Phys.*, 50, 763, 1988.
- Wilson, B.D., A.J.Mannucci, and C.D.Edwards, Sub-daily northern hemisphere maps using the IGS GPS network, *Radio Sci.*, 30, 639, 1995.
- Yeh, K.C., et al., Global ionospheric effects of the October 1989 geomagnetic storm, *J. Geophys. Res.*, 99, 6201, 1994.

Figure Captions

Figure 1. Six hour data coverage which shows the trajectories of ray paths intercepting with the ionosphere. The data interval is 18-24 UT, November 4, 1993. In the equatorial and southern hemispheric regions, there is less coverage because of fewer receivers.

Figure 2. a) Three days of Dst index data for the November 93 storm. Inserted crosses give the time and magnitude of ionospheric TEC enhancements. b) TEC enhancement occurrence rates.

Figure 3. The quiet-time ionospheric TEC map at 00-01 UT from an average of 5 quiet-time days between Oct. 29 and November 2, 1993 prior to the storm. White dots give the location of available GPS stations, white lines indicate the expected position of storm-time auroral ovals.

Figure 4. Global ionospheric TEC map at 05 - 06 UT, November 4, 1993. During this interval, the positive phase of the ionospheric storm reached its maximum in the northern hemisphere.

Figure 5. Three difference ionospheric TEC maps, respectively, at 00 - 01 UT (a), 07 - 08 UT (b), and 15 - 16 UT (c), November 4, 1993. Percent changes of storm time ionospheric TEC relative to quiet time are shown. The TEC enhancements first appear at high latitudes. Middle latitudes are affected later. After 15 hours of positive phase, depletion starts at northern hemisphere high latitudes.

Figure 6. TEC profile measured by TOPEX along the satellite trajectory during November 4 storm. TEC values interpolated from GPS measurements and calculated from the Bent model are also shown along the trajectory.

Figure 7. (a) Ionospheric peak density N_mF_2 measured between November 3 and 6, 1993 at 5 northern European ionosonde stations located roughly along a 15°E longitude. (b) TEC values from GIM along the 15°E longitude at the same latitudes as the ionosonde stations. The inserted dashed lines indicate local noon, and the solid line gives the storm start time. The correlation coefficients between both measurements are also shown in the right panel.

Figure 8. Percent changes of storm ionospheric TEC relative to quiet time in the northern hemisphere along the Greenwich meridian line. The vertical line marks the start time of the storm main phase. The ionospheric storm appears clearly at high latitude ($> 50^\circ\text{N}$ gm).

Figure 9. a) The Dst index during the November 94 storm. The inserted crosses show the TEC enhancement magnitudes. b) The TEC enhancement occurrence rate.

Figure 10. Four northern hemisphere polar view difference maps for November 94 storm. (a) at 09 - 10 UT, after storm onset, the enhancements appear in polar region; (b) at 11 - 12 UT, the enhancements develop and dayside TID moves equatorward; (c) at 13 - 14 UT the ionospheric perturbations reach their maximum; (d) at 15 - 16 UT, the TID decays and stops at $\sim 50^\circ\text{N}$ latitude.

Figure 11. A TEC difference map at 22 UT, November 26, 1994. Conjugate latitude enhancements at auroral latitudes around midnight are a clear feature. Around 21 LT, latitudinal structure from the northern hemisphere extends to the southern hemisphere.

Figure 12. A comparison of three day profiles of TEC from GIMs and N_mF_2 from three northern European ionosonde stations. N_mF_2 measurements from three ionosonde stations have features similar to those from GIMs. The correlation coefficients between both measurements are shown in the right panel.

Figure 13. The trajectory of the TID of November 26, 1994. The data points show the location and longitudinal uncertainty of the TID peak as estimated from TEC difference maps for the period 0900 - 1600 UT. The dashed curve represents a trajectory that conserves angular momentum according to equation (3) with $\phi_0 = 18^\circ$, $k = 4.69$, and using the observed values of latitude. The dotted curve represents the trajectory that the TID would have followed if it had remained at fixed local time while moving southward at the same rate as observed.

Table 1. GPS Receiver Names and Locations (1993-1994)

| Station Name (Abbr.) | Geographic Latitude | Geographic Longitude | Geomagnetic Latitude | Geomagnetic Longitude |
|-------------------------|------------------------|-------------------------|-------------------------|--------------------------|
| ALBH | 48.39 | 236.51 | 54.20 | -64.36 |
| ALGO | 45.96 | 281.93 | 56.87 | -9.12 |
| AOA1 | 34.16 | 241.17 | 41.08 | -54.57 |
| BOR1 | 52.28 | 17.07 | 51.31 | 102.01 |
| BRMU | 32.37 | 295.30 | 43.32 | 7.22 |
| BRUS | 50.80 | 4.36 | 52.31 | 89.10 |
| CARR | 35.89 | 239.57 | 42.53 | -56.74 |
| CAS1 | -66.28 | 110.52 | -77.30 | -177.38 |
| CASA | 37.64 | 241.10 | 44.49 | -55.56 |
| CIT1 | 34.14 | 241.87 | 41.17 | -53.80 |
| DAV1 | -68.58 | 77.97 | -76.78 | 124.35 |
| DRAO | 49.32 | 240.38 | 55.75 | -60.50 |
| EISL | -27.15 | 250.62 | -18.34 | -35.68 |
| FAIR | 64.98 | 212.50 | 65.26 | -100.59 |
| FORT | -3.88 | 321.57 | 5.42 | 32.56 |
| GODE | 39.02 | 283.17 | 49.97 | -7.15 |
| GOLD | 35.43 | 243.11 | 42.62 | -52.78 |
| GRAZ | 47.07 | 15.49 | 46.62 | 98.20 |
| HART | -25.89 | 27.71 | -27.02 | 93.14 |
| HARV | 34.47 | 239.32 | 41.09 | -56.64 |
| HERS | 50.87 | 0.34 | 53.15 | 85.13 |
| JPLM | 34.20 | 241.83 | 41.23 | -53.87 |
| KERG | -49.35 | 70.26 | -57.32 | 130.84 |
| KIRU | 67.86 | 20.97 | 65.07 | 116.67 |
| KIT3 | 39.13 | 66.89 | 30.64 | 142.72 |
| KOSG | 52.18 | 5.81 | 53.35 | 91.22 |
| KOUR | 5.25 | 307.19 | 15.71 | 18.75 |
| MAC1 | -54.50 | 158.94 | -60.54 | -115.53 |
| MADR | 40.43 | 355.75 | 43.96 | 76.17 |
| MAS1 | 27.76 | 344.37 | 33.61 | 60.85 |
| MATE | 40.65 | 16.70 | 40.20 | 97.03 |
| MCMU | -77.85 | 166.68 | -78.85 | -66.81 |
| MDO1 | 30.68 | 255.99 | 39.68 | -37.62 |
| METS | 60.22 | 24.40 | 57.47 | 113.10 |
| NLIB | 41.77 | 268.43 | 51.93 | -25.27 |
| NYAL | 78.93 | 11.87 | 75.45 | 130.71 |
| OATT | 34.33 | 241.40 | 41.29 | -54.36 |
| ONSA | 57.40 | 11.93 | 57.11 | 100.08 |
| PAMA | -17.57 | 210.43 | -15.10 | -75.51 |
| PERT | -31.80 | 115.89 | -42.73 | -172.13 |
| PIE1 | 34.30 | 251.88 | 42.76 | -42.87 |
| QUIN | 39.97 | 239.06 | 46.44 | -58.47 |
| RCMS | 25.61 | 279.62 | 36.47 | -10.64 |
| STJO | 47.60 | 307.32 | 57.91 | 23.40 |
| TAIW | 25.02 | 121.54 | 14.24 | -168.38 |
| TIDB | -35.40 | 148.98 | -43.48 | -133.91 |
| TMGO | 40.13 | 254.77 | 48.88 | -40.96 |
| TROM | 69.66 | 18.94 | 67.01 | 117.16 |
| TSKB | 36.11 | 140.09 | 26.49 | -152.30 |
| USC1 | 34.02 | 241.71 | 41.03 | -53.95 |
| USUD | 36.13 | 138.36 | 26.37 | -153.85 |
| WETT | 49.14 | 12.88 | 49.11 | 96.59 |
| WLSN | 34.23 | 241.94 | 41.27 | -53.75 |
| YARI | -29.05 | 115.35 | -39.99 | -172.86 |
| YELL | 62.48 | 245.52 | 69.15 | -63.46 |

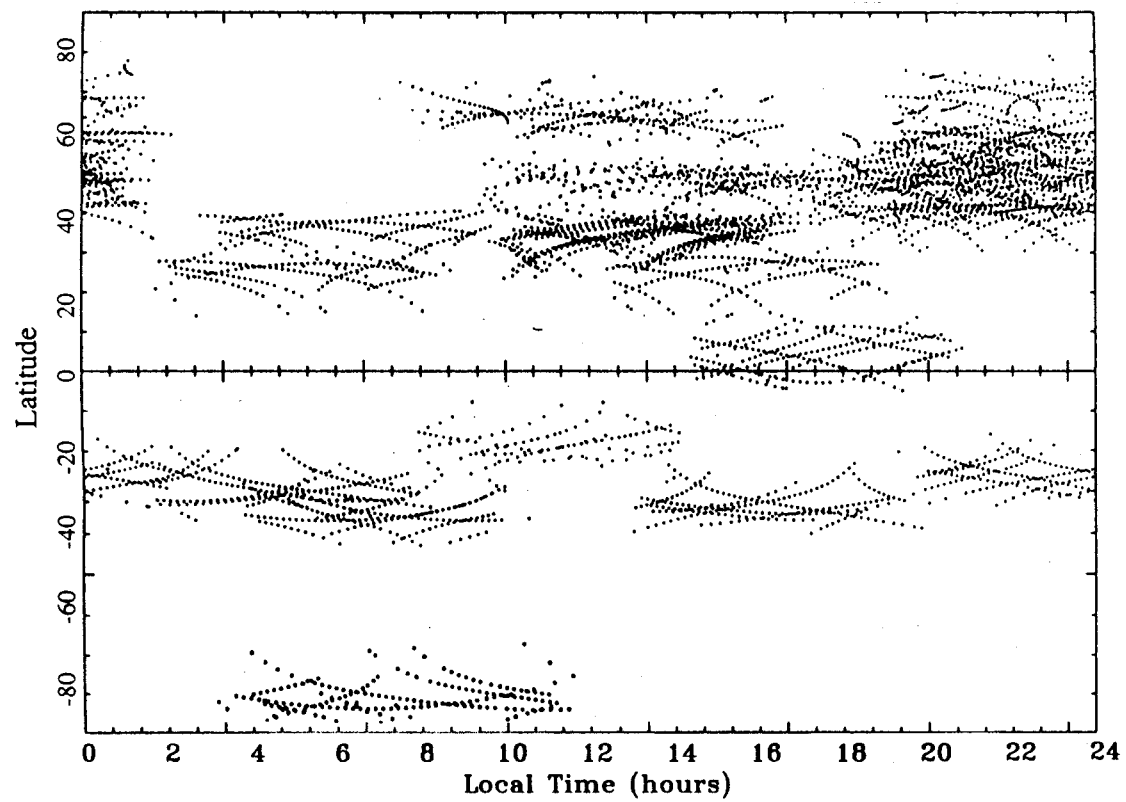


Figure 1

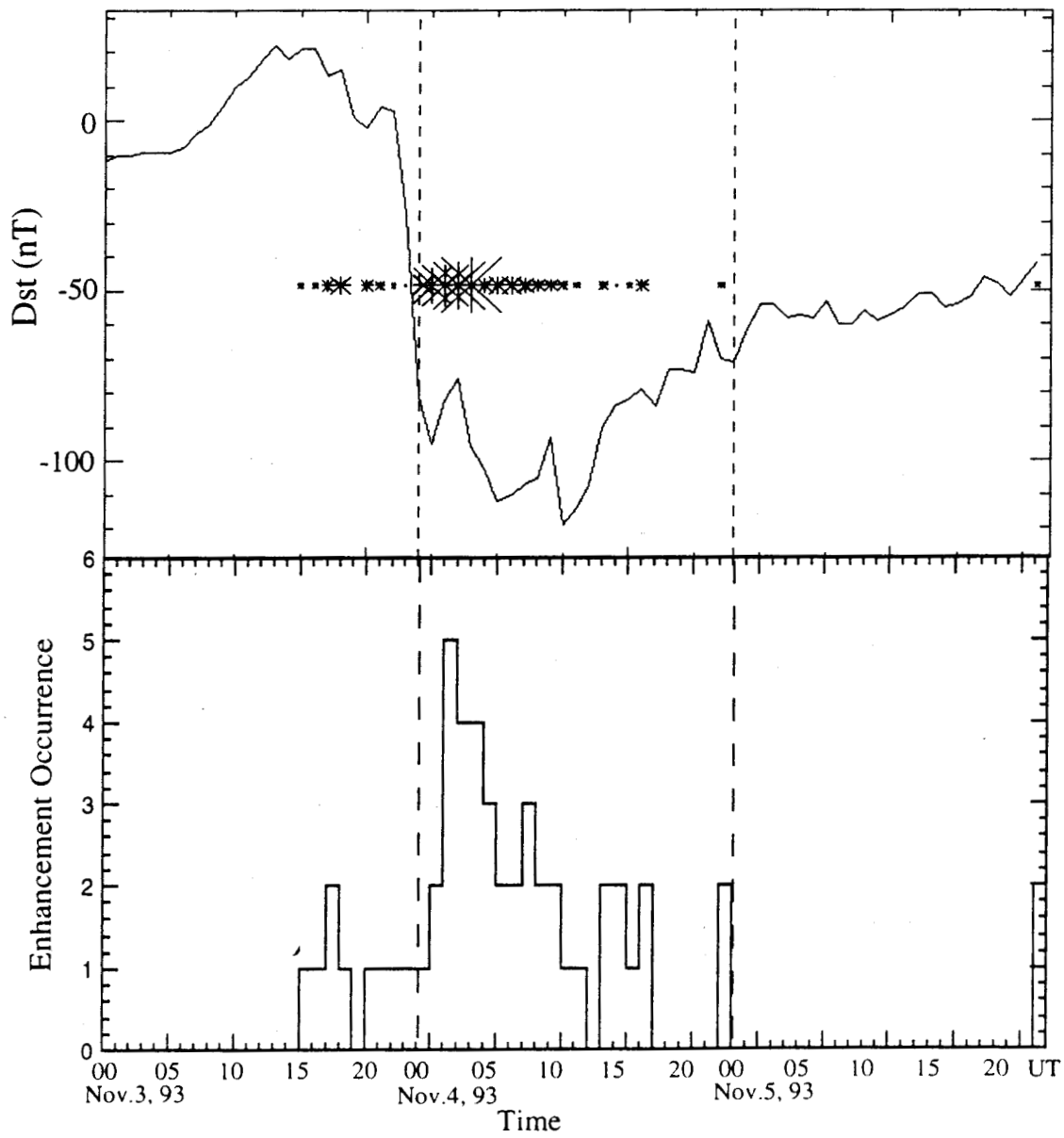


Figure 2

Date: Oct.29-Nov.02, 1993
Time: 0000-0100UT

Quiet-Time Average Ionospheric TEC Map

IPL

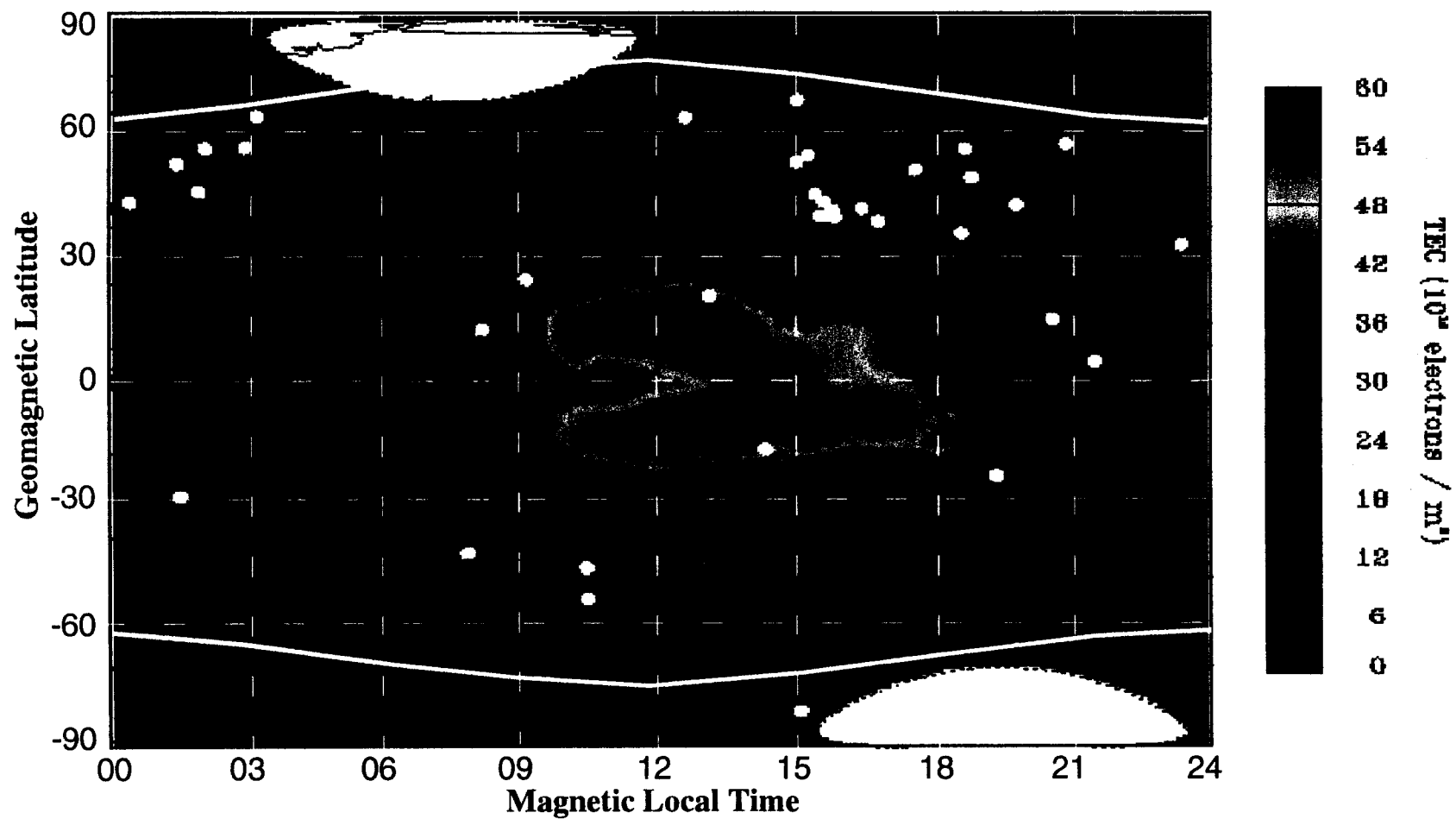


Figure 3

Date: 11/04/93
Time: 0500-0600UT

Global Ionospheric TEC Map

JPL

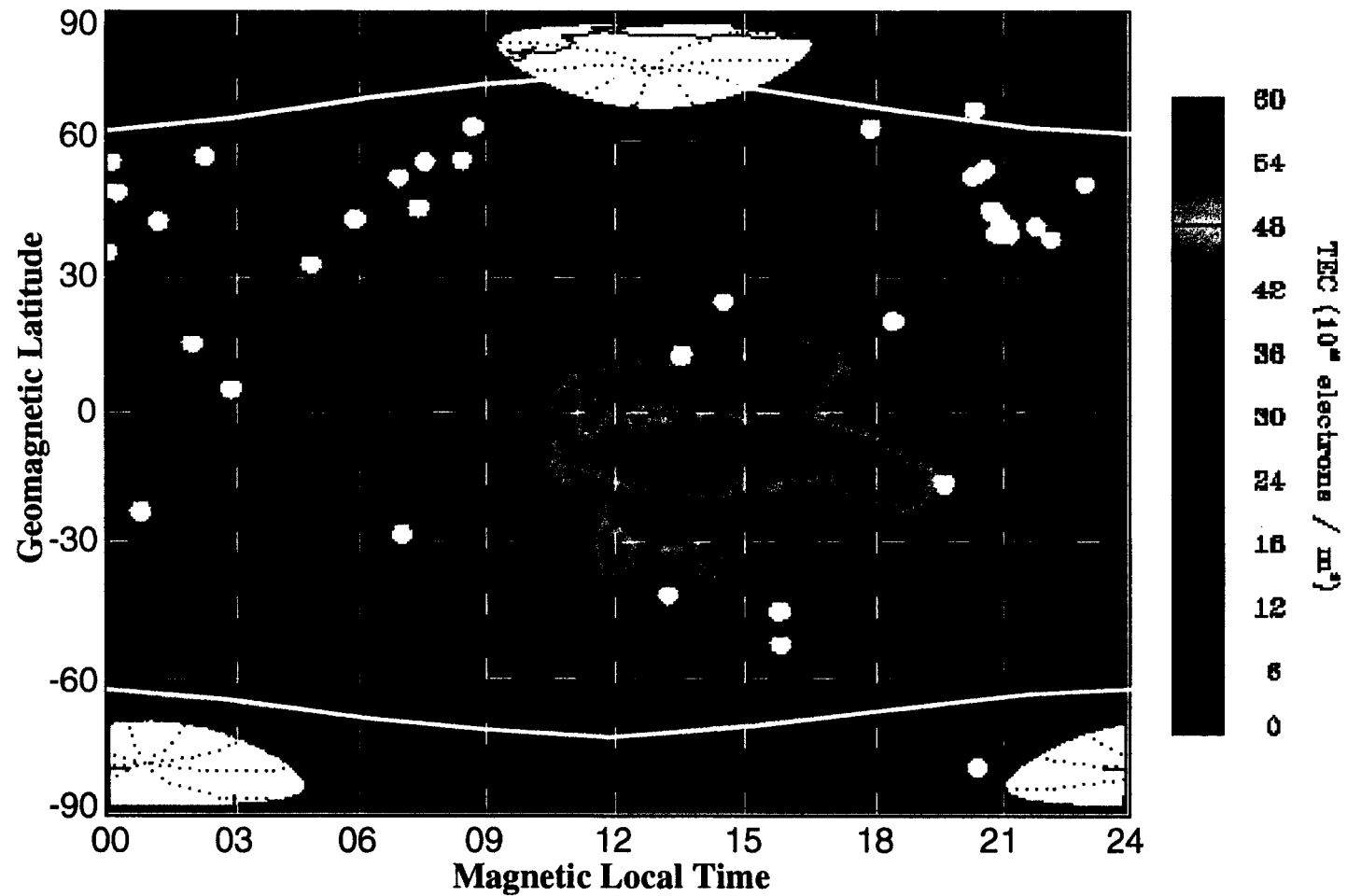


Figure 4

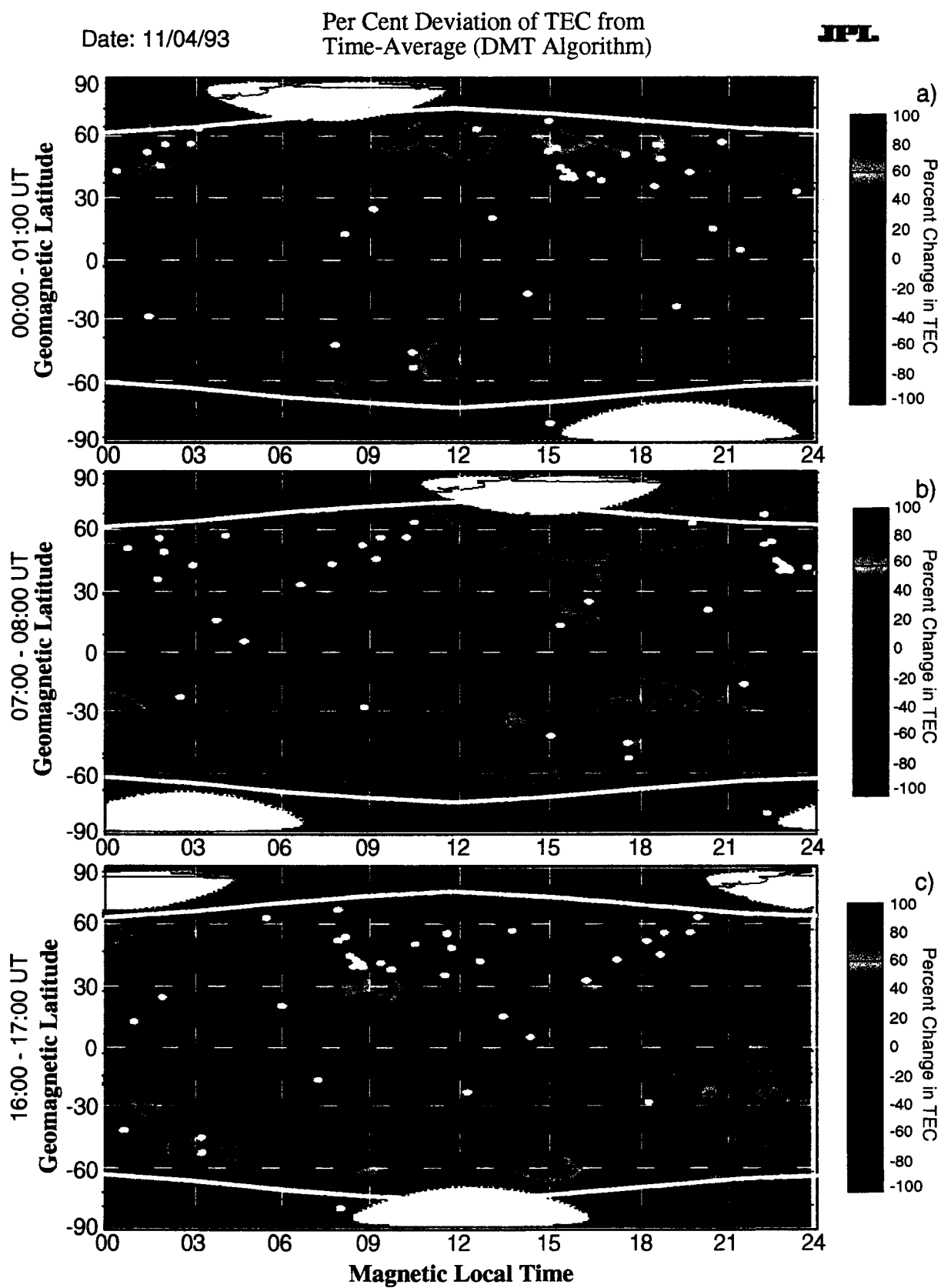


Figure 5

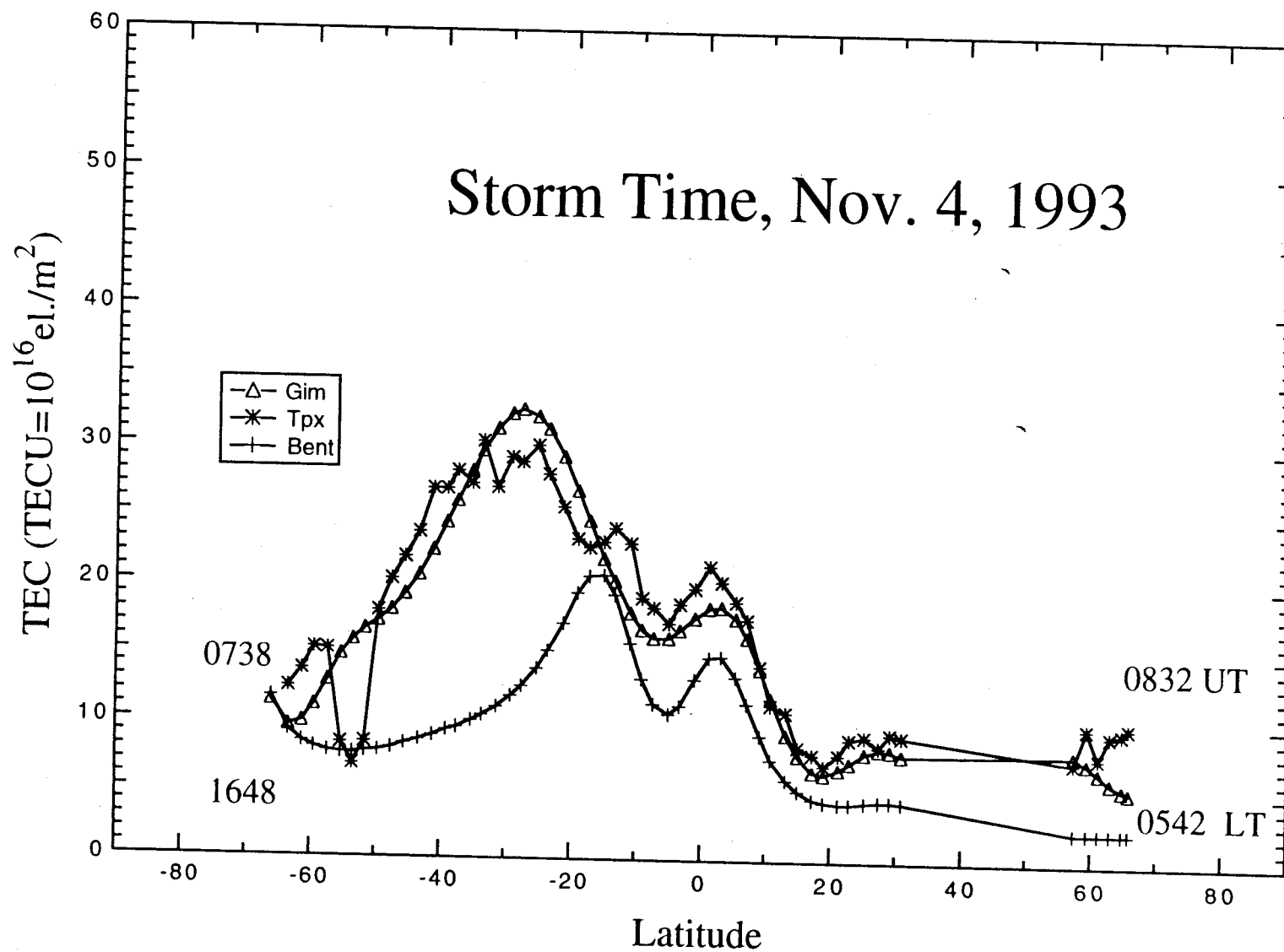


Figure 6

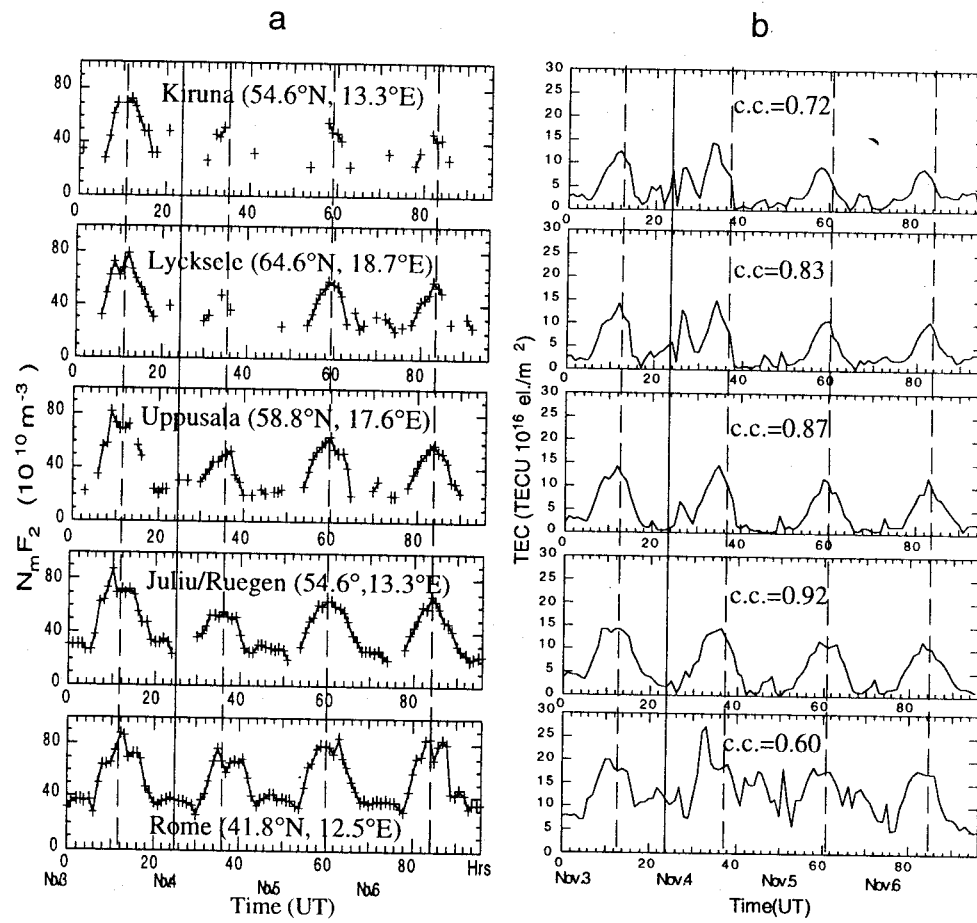


Figure 7

TEC Variations in the Northern Hemisphere along 0° Longitude

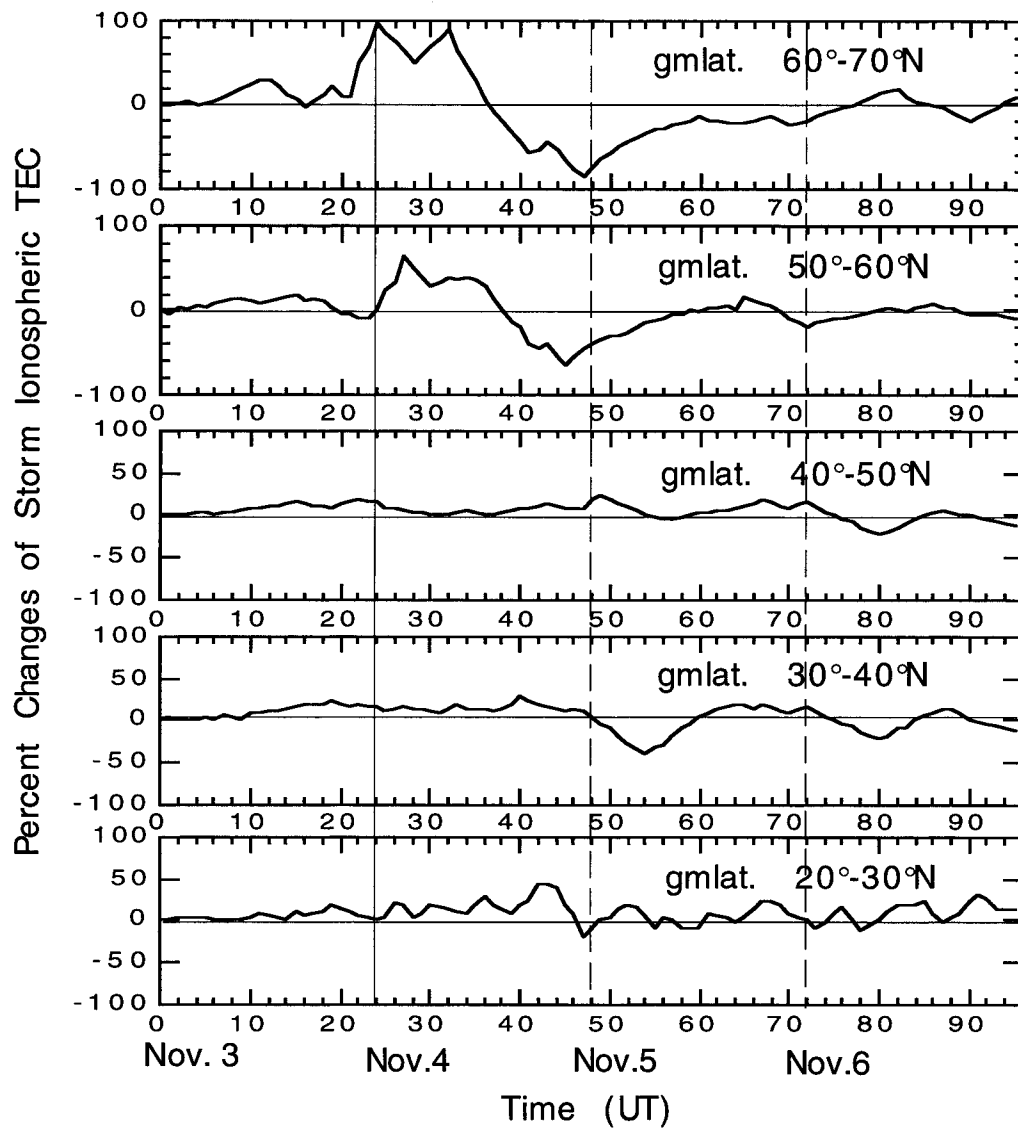
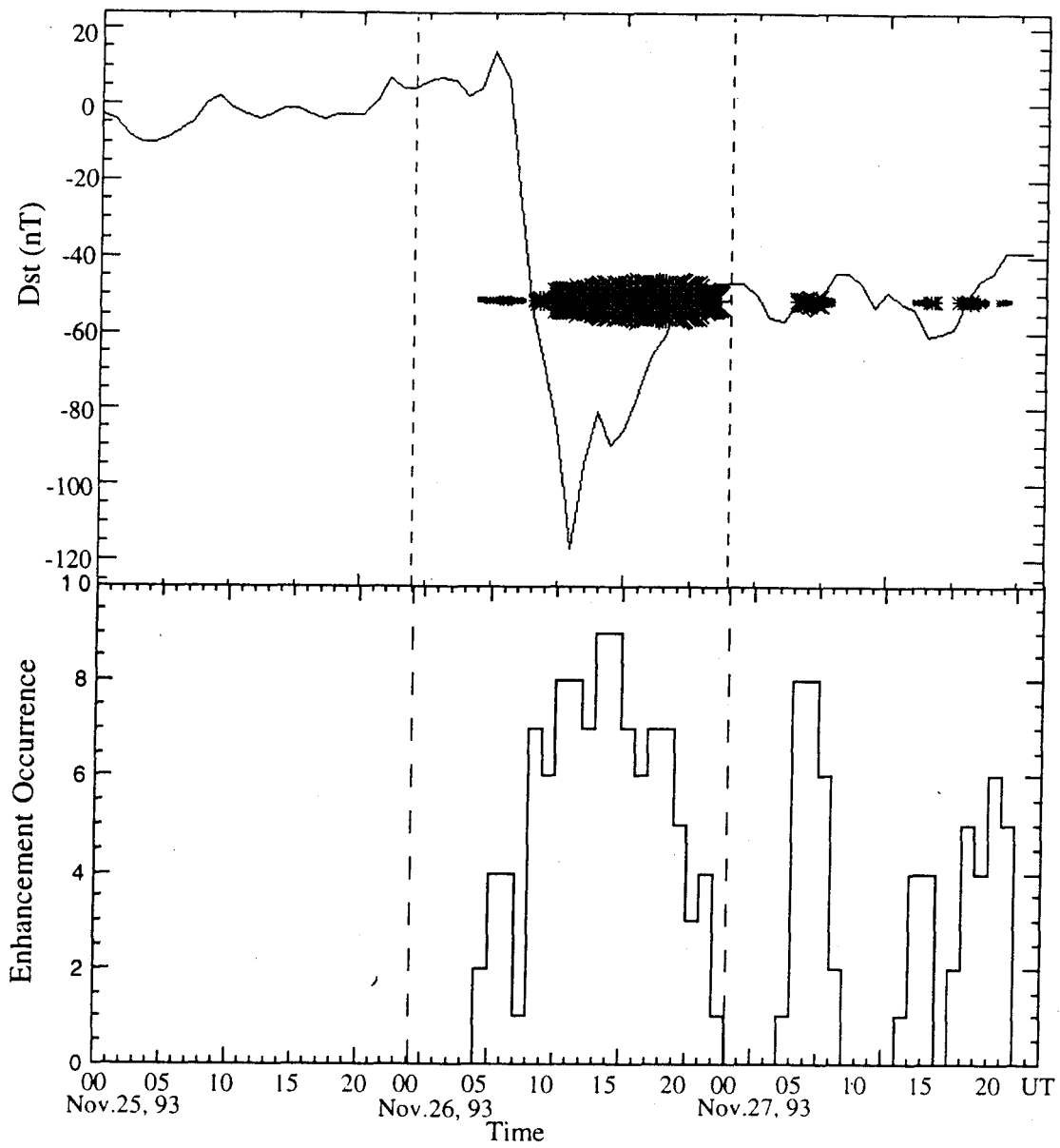


Figure 8



a)

b)

Figure 9

Per Cent Deviation of TEC from
Time-Average (DMT Algorithm)

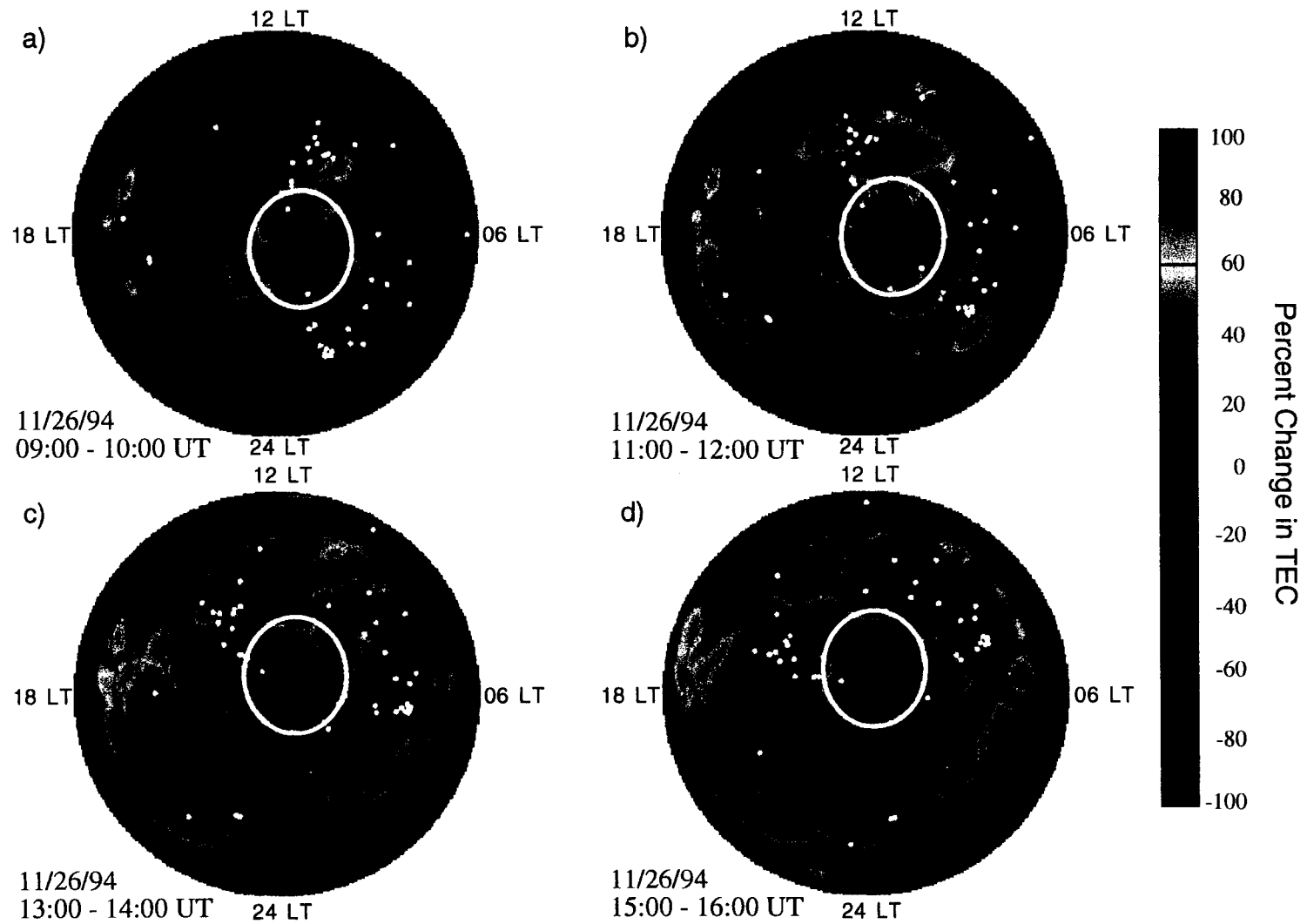


Figure 10

JPL

Date: 11/26/94
Time: 2200-2300 UT

Global Percent Change in TEC from Quiet Time Profile

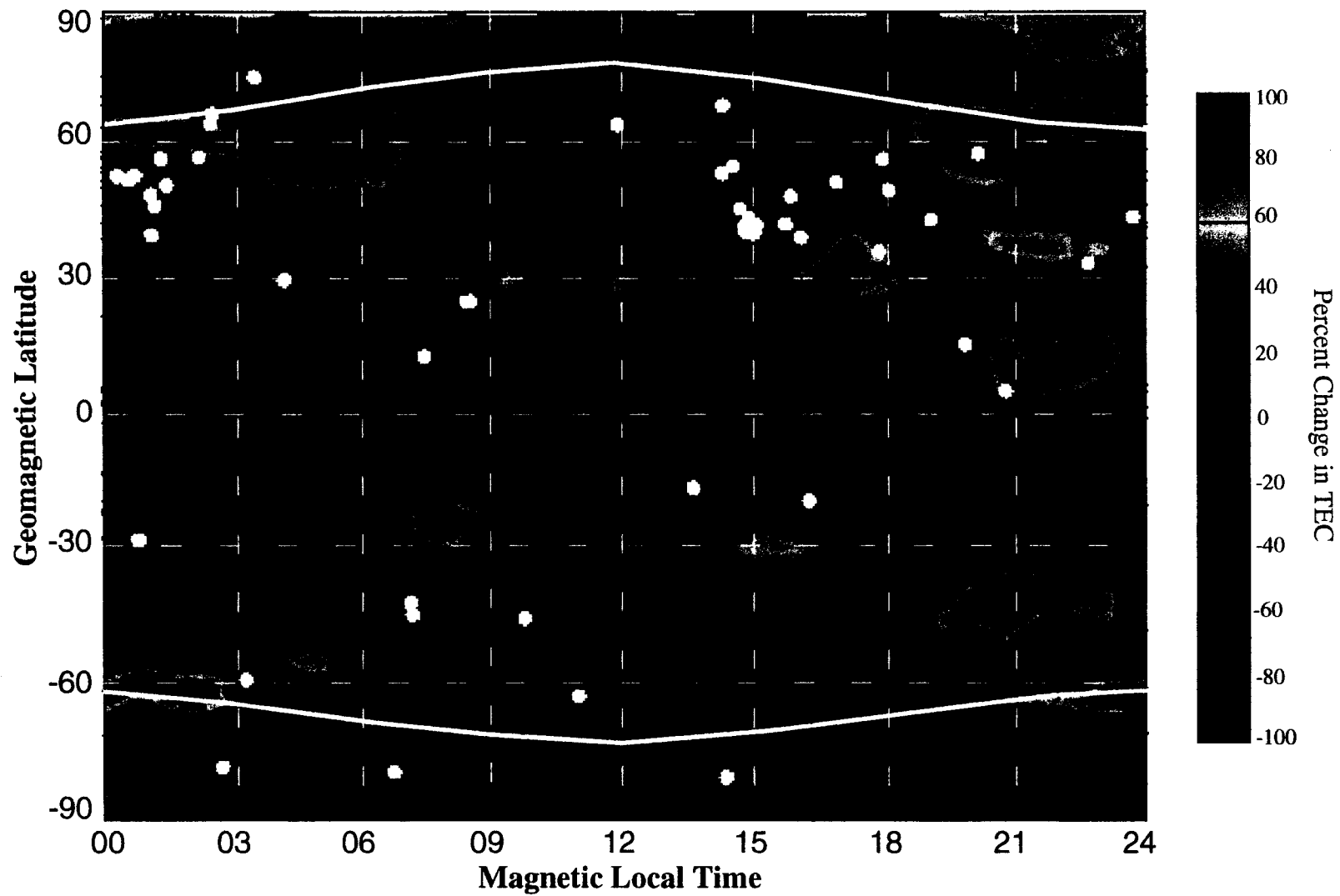


Figure 11

COMPARISON OF GPS (GIM) AND IONOSONDING MEASUREMENTS IN THREE LATITUDES

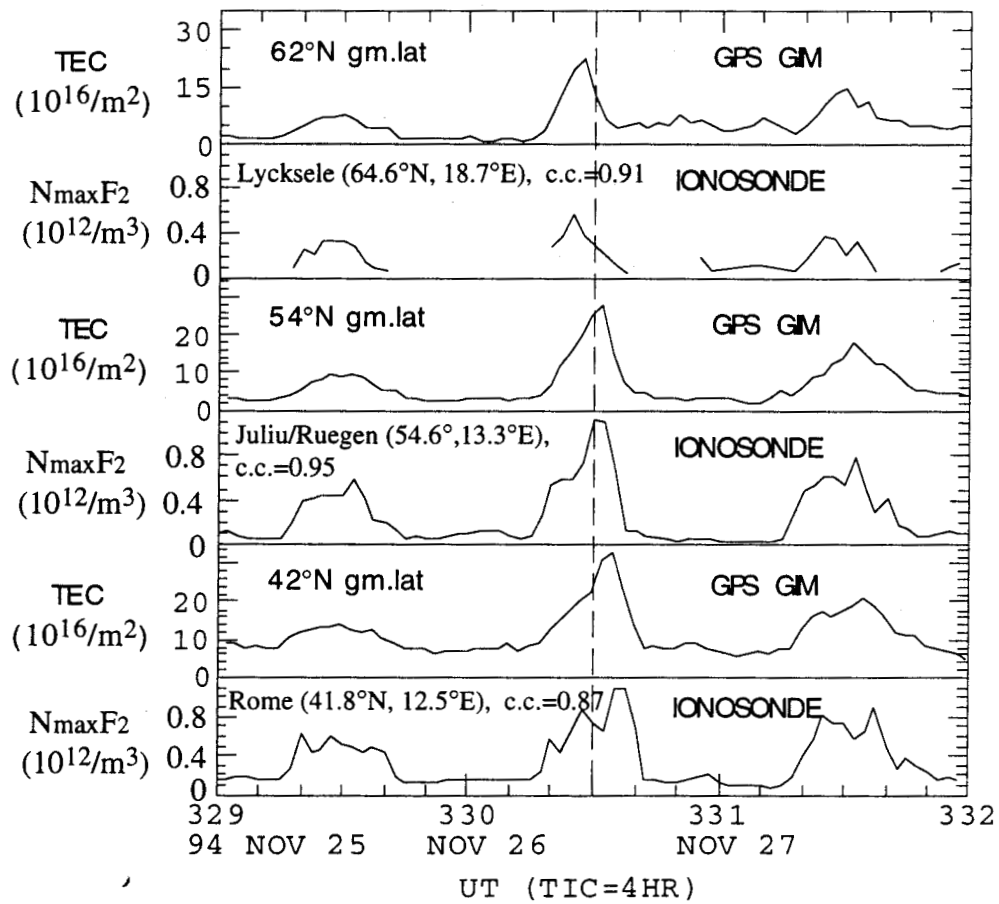


Figure 12

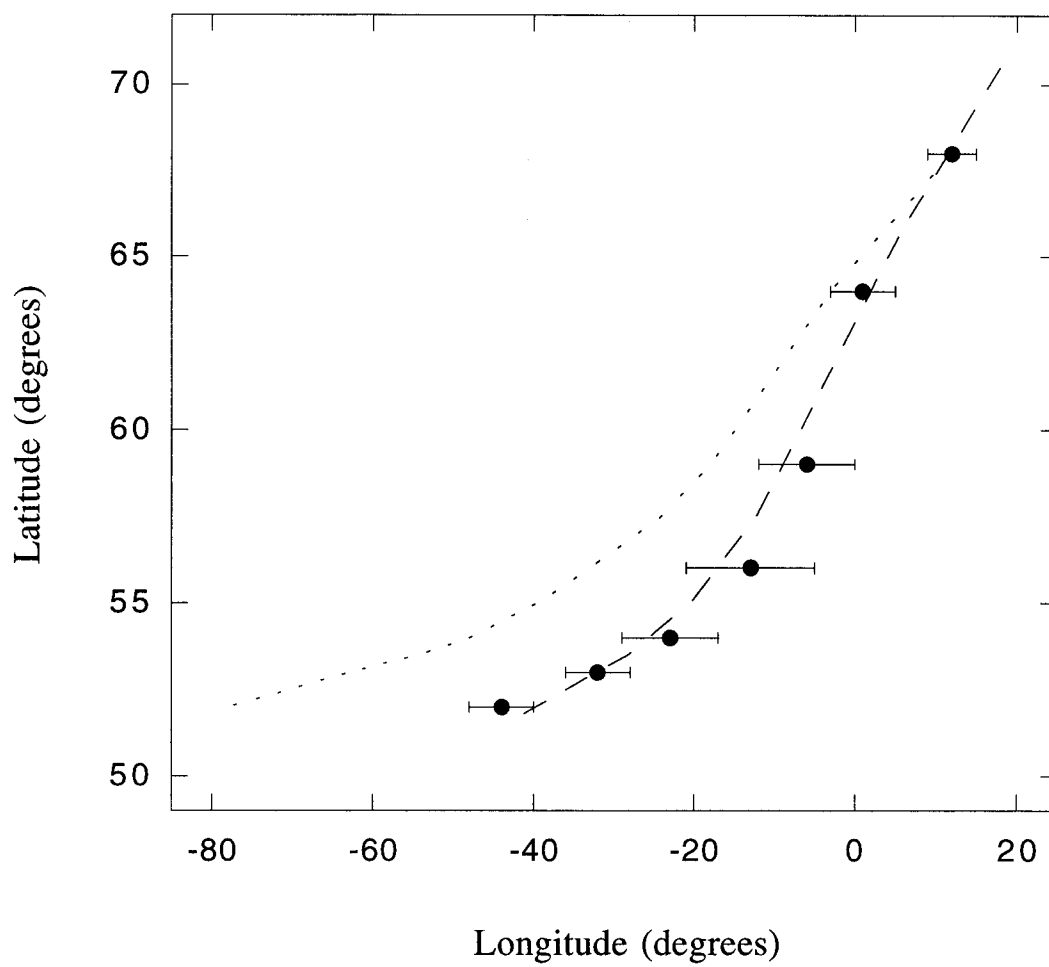


Figure 13